ACS OMEGA

Open Access



http://pubs.acs.org/journal/acsodf

Article

# Numerical Simulation of Solvent Evaporation in a Reactive Silver Ink Droplet Deposited on a Heated Substrate

Weipeng Zhang, Jun Yang, and George K. Knopf*

Cite This: *ACS Omega* 2023, 8, 38991−39003

Read Online

ACCESS | Metrics & More | Article Recommendations | Supporting Information

**ABSTRACT:** Understanding the movement of silver ions ($Ag^+$) in the solvent of a thermally evaporated particle-free reactive silver ink droplet is essential for optimizing the electronic inkjet printing process. In this work, a numerical study based on the Navier−Stokes equations is used to examine the microflows inside the evaporating solvent of a reactive silver ink droplet and to predict the morphology of the resultant Ag particle aggregations that form during the heat-activated processes. The droplet evaporation of the water−ethylene glycol ink solvent ($H_2O-(CH_2OH)_2$) is simulated using COMSOL Multiphysics software. The model assumes that the evaporating fluid is heterogeneous due to the mass transfer of ethylene glycol molecules throughout the droplet by capillary flow. A layer of concentrated ethylene glycol forms at the fluid−substrate interface during solvent evaporation if the substrate is heated. The concentrated ethylene glycol molecules are then transported inward by the capillary action, and the resultant Ag particles, arising from the thermally driven reactions, accumulate at the bottom center of the drying droplet. The numerical simulations demonstrate that the droplet evaporation process depends on the water concentration in the solvent, substrate temperature, surface tension, and natural convection. Furthermore, the capillary flow dominates the fluid flow inside the evaporating droplet, causing some Ag particles to accumulate at the contact line, the commonly observed "coffee-ring effect". The results provide new insights into the chemical reactions that produce experimentally observed silver particle aggregations during the reactive silver ink droplet evaporation process and help establish realistic process parameters for improving the quality of inkjet-printed conductive silver films and electronic circuit microtraces.

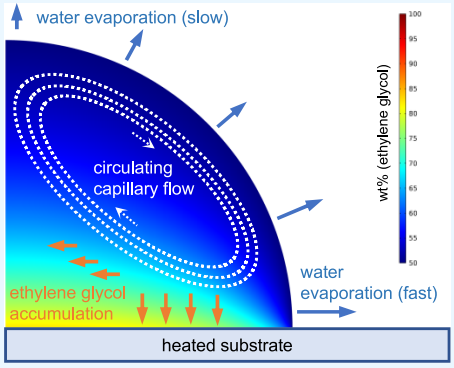


## INTRODUCTION

The evaporation behavior of a sessile liquid droplet is influenced by several complex physicochemical phenomena, including phase distinction,[1,2] internal flows,[1−5] and flow-driven distributions in temperature,[4] density,[5] and constituent component concentration.[5,6] The particle transport within the droplet during this solvent evaporation process can also produce a variety of dried film morphologies.[2,4,7] In general, the fluid flows during evaporation influence the reactions inside the droplet via mass[8] and heat transfer.[9] Therefore, understanding the internal mechanisms of solvent droplet evaporation is essential in advancing a wide range of diverse technologies associated with microfluidics,[2,3,10] catalysts,[11] printed electronics,[7,9,12,13] and inkjet printing.[9,14−16]

In terms of the particle-free reactive silver inks used for electronic printing applications, the solvent is a critical factor in determining how the resultant conductive silver (Ag) particles will uniformly spread on the substrate surface during heating and eventually dry to form the desired thin films.[9,13] Once the ink is deposited on the surface, thermal annealing improves the electrical conductivity, adhesion, and weathering stability. It is also necessary to select appropriate solvents with different polarities when depositing the inks onto substrates such as glass,[14,17] paper,[18,19] textiles,[9,20] and plastics.[18,21,22] The polarity and molecular structures of the solvent directly influence how the Ag particles aggregate during liquid evaporation and form different dry film morphologies (i.e., surface roughness, thickness, and uniformity).[23] Different packing arrangements of Ag particles during evaporation also significantly affect electrical conductivity.[24] One of the most common solvents used by reactive silver inks is a mixture of water and ethylene glycol ($H_2O-(CH_2OH)_2$).[25] The high surface tension of water makes the ink printable on a hydrophilic substrate, while ethylene glycol controls the droplet evaporation rate due to its high boiling point (197 °C). The droplet evaporation of the water and ethylene glycol mixture plays a significant role in controlling the internal chemical reactions, Ag particle aggregation behavior, and dried thin film properties.[26]

**Received:** May 21, 2023
**Accepted:** September 25, 2023
**Published:** October 10, 2023

Numerous experimental studies of droplet evaporation have been reported in the literature. In addition to describing the evaporation of a droplet on a smooth surface,[2,4,27−29] some researchers have investigated the role that rough substrates play in enhancing the droplet evaporation as the fluid travels through the surface features (e.g., craters) that strengthen the flows.[30] The flow convections at the fluid−air interface are also found to accelerate the evaporation rate of a droplet.[31]

When the ink is deposited on a substrate, the fluid will spread along the surface to form a droplet with an equilibrium radius. The droplet radius depends upon the surface tension.[2,14,17] At this equilibrium state, the fluid−gas and fluid−solid interfaces form an angle with the surface at the contact line (called *Young's contact angle*), determining the droplet's shape.[6,17] When a droplet evaporates under ambient conditions, the fluid and gas phases interact dynamically based on various factors, including composition,[5,32] temperature,[4] and interfacial flows.[2,5,32] As the evaporation process continues, the pinned contact line leads to a dynamic change in the contact angle and droplet shape.[32] The evaporation process at the contact line is faster than that at the apex of the droplet because the heat is transferred more efficiently between the substrate and fluid at the contact line. This transfer of heat at the contact line causes the local surface tension to be lowered. The imbalanced evaporation replenishes fluid from the apex to the contact line, resulting in fluid-transporting capillary flow.[5] Simultaneously, the lower surface tension at the contact line generates a reversing Marangoni flow, which minimizes the capillary flow action.[27] In contrast, when a droplet evaporates on a heated substrate, the contact line's surface tension is lower than the natural evaporation, generating a more robust capillary flow.[32] Moreover, the temperature at the apex becomes lower because the evaporating fluid transfers heat from the droplet to ambient air. However, the heat transfer at the apex is less efficient than at the contact line.

The coffee-ring effect is a ubiquitous phenomenon that occurs when a droplet with colloidal particles evaporates.[2,4,7] In terms of reactive silver ink, the mixture produces Ag particles during evaporation, and the internal flows within the droplet transport these particles throughout the fluid.[26] The replenishing capillary flow causes the particles to concentrate at the contact line, forming a coffee ring.[27] Sometimes, the evaporating droplet exhibits an inner ring, because the Marangoni flow from the contact line is robust enough to form a downward stream at the fluid−air interface closer to the apex. In addition, evaporating a droplet with particles of different sizes often produces an inner ring consisting of larger particles.[28] Regarding printed electronics, suppressing the coffee-ring effect is essential for obtaining a uniform film surface with optimal electrical conductivity properties.[29] Researchers have achieved a more uniform droplet evaporation process by adding surfactants,[33−35] modifying substrate surfaces,[36,37] enhancing interfacial reactions,[38] and gel-pinning.[39,40] For example, adding a surfactant to the solvent limits the capillary flow within the ink droplet and ensures a more uniform evaporation rate along the fluid−air interface,[33−35] thereby minimizing the coffee-ring effect.

Unfortunately, it is challenging to accurately describe the physical droplet evaporation behavior using only experimental observations because these techniques cannot show the underlying physical phenomena such as mass transportation, contact-line movement, temperature changes, and distribution of chemical concentrations. Furthermore, the droplet of reactive silver ink evaporates heterogeneously, generating complicated flow conditions for the Ag particles in the fluid. It is therefore necessary to utilize computational simulation software to better understand ink droplet evaporation and the impact of these process parameters on dry film formation.

These simulation studies also provide a tool for predicting droplet behaviors under different physical and chemical conditions like substrate temperature, solvent content, and substrate morphology. Numerical simulation of droplet evaporation is also helpful in observing invisible phenomena inside the droplet, including evaporating flux, chemical concentrations, heat transfers, and particle flows.[5,27] Numerical simulations of the evaporating ink droplet also provide important clues to predicting the morphology of the generated silver particle aggregations and fabricated electrically conductive thin films.[42]

In this work, a numerical study based on the Navier−Stokes equations is used to examine the fluid flow inside the evaporating $H_2O$−$(CH_2OH)_2$ solvent droplet to help predict the morphology of the Ag particle aggregations that form during the thermally driven chemical reactions. During evaporation, these solvent-dependent microflows will redistribute the reactants ($Ag^+$), surfactants, viscosity modifiers, and polymers within the droplet, leading to an uneven distribution of different-sized Ag particles on the fabricated film (Figure S1). Moreover, the uneven distribution of water and ethylene glycol within the drying droplet can alter the evaporation behavior, resulting in a central split within the dried ink droplet film (Figure S2).

The droplet evaporation of the particle-free silver ink solvent is simulated by using COMSOL Multiphysics software. The solvent model incorporates various mass ratios of water and ethylene glycol to investigate the behavior of their constituent distributions during the droplet evaporation process. The model is also used to examine evaporated ink droplets on heated substrates at various temperatures to observe the impact of different sintering temperatures. To predict the reactions when sintering the ink droplets, the simulations also consider several evaporating phenomena, including mass transfer, the cooling effect, flows, and evaporating mass flux. Furthermore, ink droplets with lower surface tensions are simulated to examine the evaporating behavior when surfactants are added to the reactive silver ink.

## SIMULATION METHODS

**Geometry of Droplet Evaporation.** Figure 1 shows the geometry of the droplet evaporation model containing a mixture of water ($H_2O$) and ethylene glycol ($(CH_2OH)_2$). The evaporation model is investigated in a 2D-axisymmetric manner and defined by four zones. The ink solvent droplet (zone 1) is represented as a quarter sphere with a radius of $a$ on a heated substrate. Zone 2 overlapping zone 4 is defined as an air atmosphere at ambient temperature (293 K) under 1 atm and is represented by another quarter sphere with a radius of $20a$. When the droplet evaporates, the gaseous water and ethylene glycol molecules diffuse into this zone, generating a component concentration gradient. Zone 3 represents the heated substrate beneath the evaporating droplet. In this study, the substrate has a width of $5a$ and a thickness of $h_0$ to ensure that heat is transferred through the solid−gas and solid−fluid interfaces. In this manner, heat from the substrate at temperature $T$ is transferred to the droplet to initiate


https://doi.org/10.1021/acsomega.3c03539
ACS Omega 2023, 8, 38991−39003

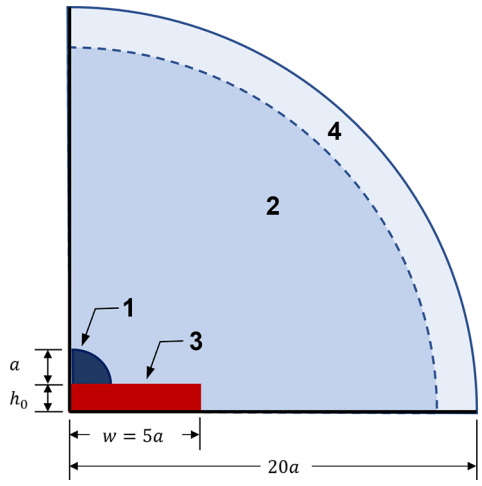


**Figure 1.** Geometry of the droplet evaporation model consisting of four zones: (1) the evaporating droplet on the substrate, a quarter sphere with a radius of $a$; (2) the air atmosphere containing vapors from the droplet and heat from the substrate and droplet, a quarter sphere with a radius of $20a$; (3) the heated substrate evaporating the droplet, in a length of $w = 5a$, and a thickness of $h_0$; (4) the infinite area indicating an open atmosphere, overlapped by zone 2. Note that the figure is not drawn to scale.

evaporation. Zone 4 is an infinite area of air, where the temperature and pressure are the same as in zone 2 (overlapped).

**Governing Equations, Boundary, and Initial Conditions.** The numerical model of the evaporation process uses the Navier–Stokes equation to define the incompressible fluid flows of the droplets containing water ($H_2O$) and ethylene glycol ($(CH_2OH)_2$) and is mathematically given by

$$\nabla \cdot u = 0 \tag{1}$$

$$\rho\left[\frac{\partial u}{\partial t} + (u\cdot\nabla u)\right] = -\nabla P + \nabla\cdot(\mu\nabla u) + f_\sigma \tag{2}$$

where $u$ is the flow velocity, $\rho$ is the density, $\mu$ is the dynamic viscosity, and $f_\sigma$ is the surface tension force per unit volume.

In this application, it is also important to incorporate the temperature distribution along the fluid–air interface. The heat transfer mechanism, or energy convection, within the droplet and air, can be represented as

$$\rho C_P\left(\frac{\partial \rho}{\partial t} + u\nabla T\right) = \nabla\cdot(k\nabla T) \tag{3}$$

while the energy convection on the substrate is given by

$$\rho C_P\frac{\partial \rho}{\partial t} = \nabla\cdot(k\nabla T) \tag{4}$$

where $t$ is the time, $C_P$ is the specific heat coefficient, and $k$ is the thermal conductivity of the fluid.

The boundary conditions for the temperature parameters used in this simulation study are

$$T = T_\infty \text{ at ambient temperature}(293.15\ \text{K}) \tag{5}$$

$$T = T_w \text{ at } z = 0,\ 5a < r < 20a \tag{6}$$

$$\Delta H = -J_w L_w - J_e L_e \text{ at } z = h_0 + h(r, t) \tag{7}$$

$$T_f = T_a \text{ at } z = h(r, t) \tag{8}$$

$$T_f = T_s - k_f\nabla T_f = -k_s\nabla T_s \text{ at } z = h_0 \tag{9}$$

where $J_w$, $J_e$, $L_w$, and $L_e$ are the evaporating mass flux and latent heat coefficients for water and ethylene glycol, respectively. The parameters $T_\infty$, $T_a$, $T_w$, $T_f$, and $T_s$ are the infinite area, ambient, wall, fluid, and substrate temperatures, respectively. The thermal conductivities of the fluid and substrate are given by $k_f$ and $k_s$, respectively. Note that eq 7 defines the cooling effect of evaporation as a boundary heat source at the fluid–air interface.

The molar fractions of water ($x_w$) and ethylene glycol ($x_e$) in the droplet volume are initially calculated using

$$x_w = \frac{n_w}{n_w + n_e} \tag{10}$$

$$x_e = \frac{n_e}{n_w + n_e} \tag{11}$$

while the mole numbers for water ($n_w$) and ethylene glycol ($n_e$) are given by

$$n_e = \oint_V c_e dV \tag{12}$$

$$n_w = \frac{V - n_e v_e}{v_w} \tag{13}$$

In the above equations, $c_e$ is the molar concentration of ethylene glycol, $V$ is the droplet's volume, $v_e$ is the molar volume of ethylene glycol (55.9 $cm^3\cdot mol^{-1}$), and $v_w$ is the molar volume of water (18.0 $cm^3\cdot mol^{-1}$). Since molecular interactions between the hydroxyl groups in ethylene glycol and water will occur in a real solution, it is necessary to also consider the impact of *mixing thermodynamics* when modeling the mass transfer within the evaporating droplet. The mass transfer boundary conditions for mixing thermodynamics are incorporated in the simulation using the Maxwell–Stefan diffusion equations

$$\rho\frac{\partial \omega_e}{\partial t} + \nabla j_e + \rho(u\cdot\nabla)\omega_e = 0 \tag{14}$$

$$j_e = -\left(\rho\omega_e\sum_w D'_{we}d_w + D_e^T\frac{\nabla T}{T}\right) \tag{15}$$

$$d_w = \nabla x_w + \frac{1}{P_A}(x_w - \omega_w)\nabla P_A \tag{16}$$

$$x_w = \frac{M_e\omega_w}{M_w\omega_e} \tag{17}$$

where $j_e$ is the relative mass flux of ethylene glycol in the Maxwell–Stefan diffusion model; $D'_{we}$ is the multicomponent Fick diffusivity; $d_w$ is the diffusional driving force of water; $D_e^T$ is the diffusion coefficient of ethylene glycol at the temperature $T$; $P_A$ is the air pressure using 1 atm in the models; $\omega_e$ and $\omega_w$ are the mass fractions (called concentrations) of ethylene glycol and water; and $M_e$ and $M_w$ are the molecular weights of ethylene glycol and water.

The density ($\rho$) and mass fraction ($\omega_e$, $\omega_w$) during the thermodynamic mixing process are calculated using

$$\rho = \frac{1}{\frac{\omega_e}{\rho_e} + \frac{\omega_w}{\rho_w}} \tag{18}$$



https://doi.org/10.1021/acsomega.3c03539
ACS Omega 2023, 8, 38991−39003

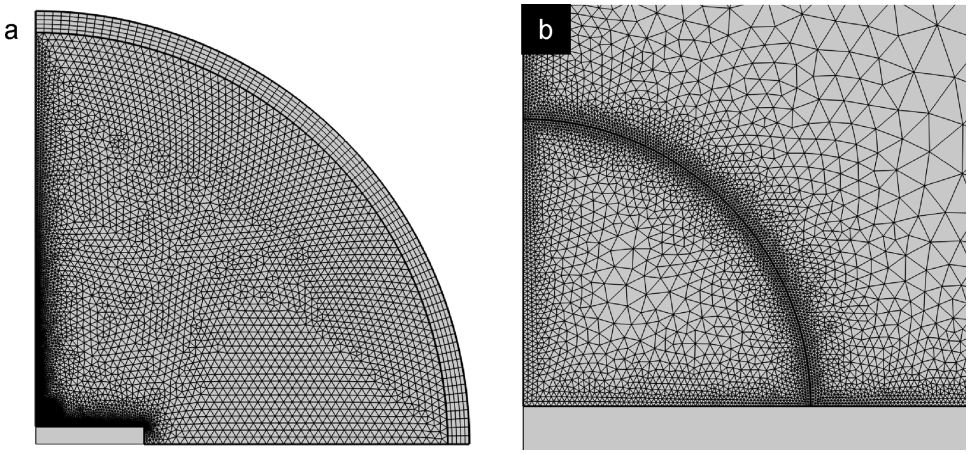


**Figure 2.** Mesh designed for the evaporation model: (a) mesh of the whole model, which was dense within the droplet and the above vertical atmosphere; (b) detailed mesh near the droplet area, showing a further dense mesh on the fluid−air interface.

$$\omega_e = \frac{c_e M_e}{c_e M_e + c_w M_w}, \quad \omega_w = \frac{c_w M_w}{c_e M_e + c_w M_w} \tag{19}$$

where $c_e$ and $c_w$ are the concentrations of ethylene glycol and water within the droplet.

In addition, the evaporating mass fluxes of water and ethylene glycol are determined by

$$J_w = - M_w D_w \nabla_n c_{v,w} \tag{20}$$

$$J_e = - M_e D_e \nabla_n c_{v,e} \tag{21}$$

where $D_w$ and $D_e$ are the diffusion coefficients of water and ethylene glycol molecules in the air, $\nabla_n$ is the normalized derivative at the fluid−air interface, and $c_{v,w}$ and $c_{v,e}$ are the concentrations of water and ethylene glycol in the vapor.

The Navier−Stokes and continuity equations are the boundary equations for natural convection involved in nonisothermal simulations and are given by

$$\frac{\partial \rho_A}{\partial t} + \nabla \cdot (\rho_A u) = 0 \tag{22}$$

$$\rho_A \left( \frac{\partial u}{\partial t} + u \cdot \nabla u \right) = - \nabla P + \nabla \cdot \left( \mu (\nabla u + (\nabla u)^T) - \frac{2}{3} \mu (\nabla \cdot u)_I \right) + \rho_A g \tag{23}$$

where $\rho_A$ is the density of air varied with temperature.

Finally, the convection−diffusion equation with flow velocity ($u$) is determined by solving

$$\frac{\partial \rho_{v,w}}{\partial t} + u \cdot \nabla c_{v,w} = \nabla \cdot (D_{v,w} \nabla c_{v,w}) \tag{24}$$

$$\frac{\partial \rho_{v,e}}{\partial t} + u \cdot \nabla c_{v,e} = \nabla \cdot (D_{v,e} \nabla c_{v,e}) \tag{25}$$

**Simulation Software and Mesh Design.** COMSOL Multiphysics is a powerful simulation tool for exploring physical phenomena with complicated process parameters. In this study, the "microfluidics" and "Heat Transfer" modules in COMSOL were adapted to meet the requirements for simulating solvent droplet evaporation on a heated substrate. The physics included different domains, such as heat, mass, flow, and phase movement. The simulation program utilized "Transport of Concentrated Species" to calculate the mass transfer within the droplet (zone 1), coping with the $H_2O$−$(CH_2OH)_2$ mixture (i.e., a nonideal solution). "Transport of Diluted Species" in the infinite air (zones 2 and 4) modeled the gaseous behavior across the fluid−air interface during the evaporation. The simulation implemented "Heat Transfer in Solid and Liquid" to evaporate the droplet at the air−substrate, fluid−substrate, and fluid−air interfaces (between zones 2 and 3, zones 1 and 3, and zones 1 and 2). As a nonideal solution, the $H_2O$−$(CH_2OH)_2$ mixture needed "Reaction Engineering" to solve the mixing thermodynamics and density during droplet evaporation (zone 1). "Laminar Flow" represents a single-phase flow within the droplet (zone 1) and air (zone 2). It solved the continuity and Navier−Stokes equations to demonstrate natural convection at the fluid−air interface. Finally, the simulation used "Moving Mesh" to operate the moving fluid−air interface of the evaporating droplet. It used the arbitrary Lagrangian−Eulerian (ALE) approach to follow the moving problem domains with the evaporation time.

The mesh was created using triangular units to discretize the problem domains and simulate the models under the boundary conditions (Figure 2). COMSOL used a fully coupled solver to obtain numerical solutions through the multifrontal massively parallel sparse direct solver (MUMPS). Zone 1 required a dense mesh, because the time-dependent fluid dynamics within the droplet were highly active and critical to the evaporation analysis (Figure 2a). The mesh density was further increased around the fluid−air interface of the droplet (Figure 2b). In other areas of the evaporation model, such as the substrate and atmospheric air (zones 2, 3, and 4), the mesh was coarser than that in zone 1 to simplify the calculations. However, the part of zone 2 located vertically above the droplet was denser than the other gaseous locations to accurately simulate the natural convection process. A finer mesh was also incorporated along the vertical axis to accommodate more robust heat flow from the substrate.

**Material Properties.** The physical properties of air, water, and ethylene glycol are generally temperature-dependent. COMSOL provided the values of the material properties and thermodynamics from its material library in the simulation. It also automatically calculated the droplet's density and concentrations of water and ethylene glycol during the thermodynamic mixing process. Furthermore, the simulations considered only glass substrates.



https://doi.org/10.1021/acsomega.3c03539
ACS Omega 2023, 8, 38991−39003

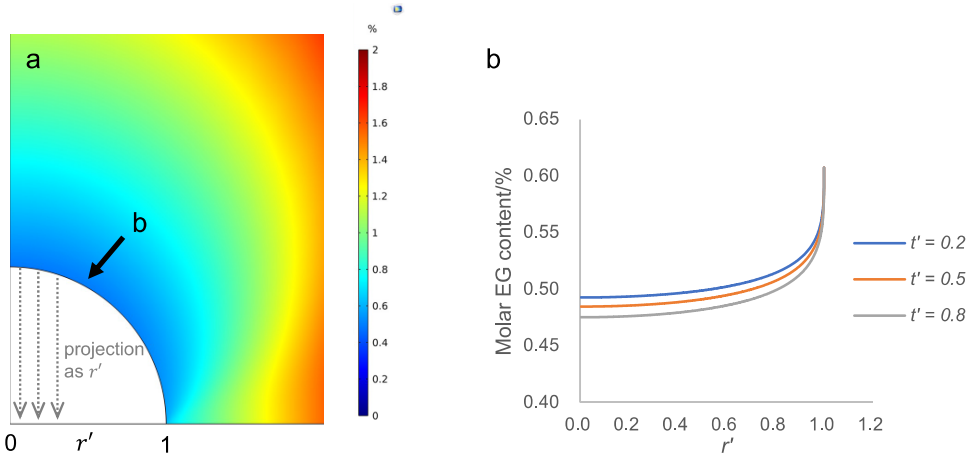


**Figure 3.** Molar fractions (mol %) of ethylene glycol ($x_e$) in the air domain at $t'$ = 0.2, 0.5, and 0.8. The droplet contained an initial 50 wt %, evaporating at 308 K: (a) fraction distribution at $t'$ = 0.5, with a rainbow legend from 0 to 2 mol %; (b) molar fractions (mol %) on the fluid−air interface. $r'$ represents the location along the fluid−air interface from the apex (0) to the contact line (1).

**Dimensional Scaling for Process Analysis.** The model uses *normalized radius* $r'$ and *normalized time* $t'$ to describe the simulated results of evaporation rates, evaporation times, and the relative locations of the fluid−substrate and fluid−air interfaces. The normalized radius is given as

$$r' = \frac{r}{R} \tag{26}$$

where $r$ is the distance from the droplet center along the fluid−substrate interface and $R$ is the radius of the evaporating droplet at a specified instant in time. Note that the radius of the droplet, $R$, decreases over time during evaporation. Equation 26 defines $r'$ from 0 (center of the droplet) to 1 (contact line). The normalized time is

$$t' = \frac{t}{t_D} \tag{27}$$

where $t$ is the time after the start of evaporation and $t_D$ is the reference time that occurs when a droplet with more than 50 wt % water has evaporated half its original volume (i.e., 50 vol %). However, the exception is the case for the droplet composed of 60 wt % ethylene glycol and 40 wt % water. Since ethylene glycol does not evaporate at the simulated temperatures, the most significant possible reduction in volume can only be 40 vol % (i.e., water concentration).

## RESULTS AND DISCUSSION

**Model Validation.** The simulation study is validated by comparing the evaporation rates with the experimental observations found in the literature.[43] The evaporation rates were determined during eight simulated droplet evaporations by calculating the mass of the fluid lost during the reference time, $t_D$. Five of the simulated droplets contained different concentrations of ethylene glycol, including 20, 30, 40, 50, and 60 wt %. The droplet was assumed to be asymmetric, and therefore, only a quarter sphere needed to be simulated with $a$ = 1.35 mm. Furthermore, the ambient temperature was $T_a$ = 293 K, and the droplets evaporated on glass substrates at $T_s$ = 308 K. The substrate was rectangular, with $h_0$ = 1.10 mm and $w$ = 5$a$ = 6.75 mm. The other three simulations involved heating the substrate to different temperatures (303, 313, and 318 K) and observing the evaporating process for droplets with an initial 50 wt % ethylene glycol.

The evaporation rate is greatly affected by the different molecular weights of water ($M_w$ = 18 g·mol$^{-1}$) and ethylene glycol ($M_e$= 62 g·mol$^{-1}$). Specifically, it is necessary to correctly describe the vapor composition by estimating the amount of ethylene glycol molecules diffusing from the liquid to the gas phase at the fluid−air interface. In this study, the molar fraction of ethylene glycol at the fluid−air interface was about $x_e \approx 0.5$ mol % (Figure 3a). Note that this is considered a low level of ethylene glycol concentration in the vapor. Note that $x_e$ increased with a greater distance from the droplet because the diffusion coefficient of water was 25 times higher than ethylene glycol.[44] Consequently, water vapor is distributed over a significantly larger volume due to fast diffusion, leading to the relatively low $x_w$. The natural convection processes will also drive the evaporated ethylene glycol molecules upward because the heated substrate is below the droplet. Furthermore, the vapor will diffuse across the fluid−air interface faster in the vertical direction due to the lower density of heated vapor than the cooler ambient air.

The molar fraction of ethylene glycol ($x_e$) at the fluid−air interface also varies with the distance from the droplet apex (Figure 3b). The simulations show $x_e$ gradually increasing from the droplet apex ($r'$ = 0) toward ($r'$ = 0.8) and then rapidly increasing to a maximum value of $x_e \approx 0.6$ mol % at the contact line ($r'$ = 1). This phenomenon implies that evaporation occurs the fastest near the contact line. The three curves in Figure 3b correspond to different normalized time instances $t'$ = 0.2, 0.5, and 0.8. As the evaporation process progressed (i.e., increasing $t'$), the molar fraction of ethylene glycol in the droplet ($x_e$) decreased because of the accelerated water evaporation at the fluid−air interface.

The evaporation rates for various molar fractions of ethylene glycol concentration in the droplets at different temperatures are compared with those taken from the published literature[43] (Figure 4). Both the COMSOL simulations and experiments exhibited a linear relationship in the evaporation rates when the ethylene glycol concentration ranged from 20 to 60 wt %. However, the calculated evaporation rates in the simulation are 20 to 40% lower than reported in the literature. These differences result from several factors, including how the temperature variations along the fluid−air interface were determined. Rusdi et al.[43] used thermal gravimetric analysis to experimentally observe the evaporation rates by uniformly


https://doi.org/10.1021/acsomega.3c03539
ACS Omega 2023, 8, 38991−39003

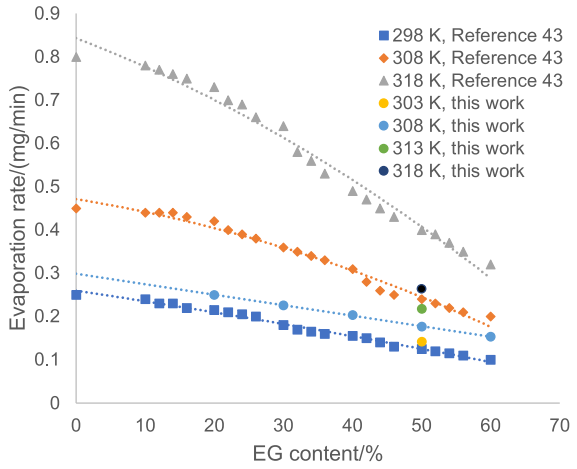


**Figure 4.** Evaporation rates ($mg \cdot min^{-1}$) of $H_2O-(CH_2OH)_2$ mixtures with different initial ethylene glycol concentrations (20, 30, 40, 50, and 60 wt % in the simulation) at different temperatures (303, 308, 313, and 318 K in the simulation), comparing the simulation with the experimental observation from ref 43. The circles were the evaporation rates in the simulation, and the triangles, squares, and diamonds were the evaporation rates from the literature.

heating the droplet fluid, including the fluid−air interface. In contrast, the COMSOL simulation model represents the evaporation of a solvent droplet exposed to ambient air and resting on a heated substrate (i.e., nonuniform heating). Note that nonuniform heating of the reactive silver ink droplet is a more common and realistic situation for electronic inkjet printing. For the simulation, the $H_2O-(CH_2OH)_2$ solvent droplets have a lower temperature than that of the heated substrate, especially the fluid located in the upper regions of the droplet near the fluid−air interface at the apex. The temperature difference between the droplet apex and the heated substrate meant that a droplet with a higher water concentration would evaporate slower than the one with less water.

It is important to note that several sources of error in the COMSOL simulations must be considered in reviewing the results. For example, the geometry of the droplet during evaporation was simplified to achieve computational efficiency. Specifically, the contact angle of the droplet does not change as it evaporates on the heated substrate. Incorporating a dynamically changing droplet mesh into the COMSOL simulations would require an immense number of calculations and a substantial increase in the computational time. Since the goal of the study was to investigate how microflows in the evaporating droplet produce the "coffee-ring effect" and not graphically visualize the evaporating droplet over time, the simplified droplet was represented as a quarter sphere with a fixed contact angle that shrank proportionately during evaporation. Another potential source of error in the simulated results is that the COMSOL software retained a small amount of extra water in the droplet after it officially evaporated (Figure S3). In addition, the computational model adjusted the diffusion of ethylene glycol by raising the diffusion coefficient in the liquid phase ($6 \times 10^{-9}$ $m^2 \cdot s^{-1}$) and decreasing the diffusion coefficient across the interface ($1.1 \times 10^{-9}$ $m^2 \cdot s^{-1}$). Although these computation errors and limitations did affect the accuracy of the results, the simulations still proved to be a realistic representation of the mass transfer, heat transfer, and microflows observed during the droplet evaporation of the reactive ink solvent.

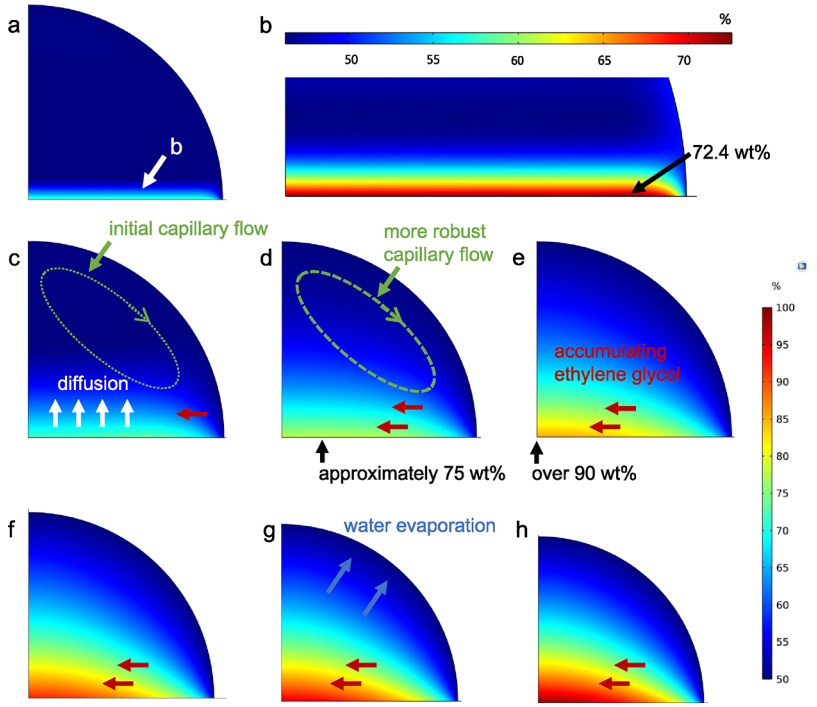


**Figure 5.** Ethylene glycol concentrations (wt %) within a droplet having an initial 50 wt %, evaporating at 308 K and *t*: (a) 1 s; (c) 15 s; (d) 30 s; (e) 60 s; (f) 240 s ($t' = 0.3$); (g) 435 s ($t' = 0.5$); (h) 696 s ($t' = 0.8$). The color bar on the left ranges the concentration from 50 wt % (dark blue) to 100 wt % (dark red). Due to the heated substrate, an ethylene glycol-accumulated layer appeared at the fluid−substrate interface. With the progressing evaporation, the capillary flow accumulated ethylene glycol at the bottom center like piling a sandhill. Panel (b) provides a detailed observation of panel (a) at the initial layer with a color bar from 45 wt % (dark blue) to 73 wt % (dark red).



https://doi.org/10.1021/acsomega.3c03539
ACS Omega 2023, 8, 38991−39003

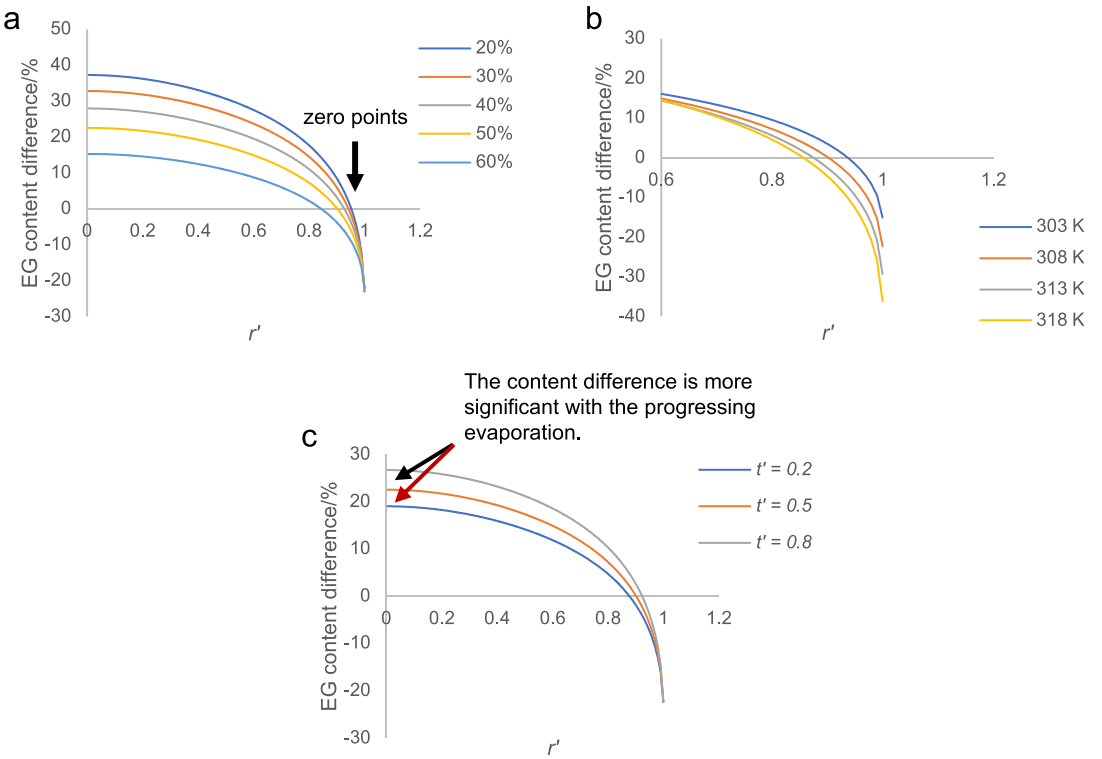


**Figure 6.** Horizontally distributive differences of ethylene glycol concentration (wt %) at the fluid−substrate interface of droplets, compared with the initial layers: (a) with different initial concentrations (20, 30, 40, 50, and 60 wt %), evaporating at 308 K and $t'$ = 0.5; (b) containing an initial 50 wt %, evaporating at different temperatures (303, 308, 313, and 318 K), $t'$ = 0.5; (c) containing an initial 50 wt %, evaporating at 308 K and $t'$ = 0.2, 0.5, and 0.8. $r'$ projects the relative location of the interface from the center (0) to the contact line (1).

**"Sandhill Piling" Analogy of Ethylene Glycol Accumulation.** The circulating capillary flow accumulates ethylene glycol at the bottom of the droplet, forming a concentrated layer at the fluid−substrate interface (Figure 5). Since the $H_2O$−$(CH_2OH)_2$ mixture is a binary solvent system, the evaporation results in the mass transfer of water and ethylene glycol within the droplet. Their concentrations change dynamically during evaporation because the heating process only removes water molecules at the fluid−air interface, while the capillary flow simultaneously replenishes fluid from the apex to the contact line.

Figure 5 demonstrates the mass transfer of ethylene glycol within a droplet that initially contained 50 wt % ethylene glycol and the substrate heated to 308 K over a series of time intervals ($t$ = 1, 15, 30, 60, 240 ($t'$ = 0.3), 435 ($t'$ = 0.5), and 696 s ($t'$ = 0.8)). The layer of ethylene glycol first appeared at the beginning of the evaporation process ($t$ = 1 s; Figure 5a). The capillary flow within the droplet pushes the layer and concentrated ethylene glycol to the bottom center, analogous to forming a sand mound. Figure 5b is an expanded view of Figure 5a ($t$ = 1 s) with additional details about the initial layer formation. Although the concentration of ethylene glycol at $t$ = 1 s is 50 wt % for the whole droplet, the layer formed at the fluid−substrate interface is 72.4 wt % ethylene glycol because the heated substrate has lowered the surface tension, causing an increased ethylene glycol concentration. This layer was formed by attracting ethylene glycol from the nearby fluid because its lower polarity favored ethylene glycol over water (Figure S4). Note that higher substrate temperatures (e.g., 318 K) will further lower the surface tension at the interface, causing a more significant accumulation of ethylene glycol.

Figure 5c shows the change in the layer at the fluid−substrate interface after 15 s. The capillary flow has accumulated more ethylene glycol at the center than previously, causing the layer to shrink inward, as indicated by the red arrow. This phenomenon arises, in part, from a more thorough heat diffusion process over 15 s. As the heating process continues for 30 s (Figure 5d), a more robust capillary flow is observed in the evaporating droplet. The layer on the fluid−substrate interface now exhibits ∼75 wt % ethylene glycol and has become thicker. At 60 s (Figure 5e), the length of the layer shrinks inward toward the center, while the height continues to increase due to the "piling" of ethylene glycol originally from the contact line. This piling process leads to a concentrated spot of ethylene glycol (over 90 wt %) near the bottom center of the droplet. With ongoing heated evaporation, a sandhill-like structure appears at the bottom center containing over 90 wt % ethylene glycol (Figure 5f−h).

The mass transfer of ethylene glycol molecules from the initial layer (Figure 5b) depends on the circulating capillary flow (Figure S5) within the droplet. The robust flow effectively collects ethylene glycol from the contact line, leading to a highly concentrated area at the bottom center. Figure 6a,b quantitatively shows the concentration differences of ethylene glycol at the fluid−substrate interface compared with the initial layers. The zero points show the locations where the concentrations equal the initial layers (Figure S6). The more robust flows concentrate, push, and elevate the accumulated ethylene glycol fluid more effectively to create a larger "sandhill-like" fluid zone. This study used $r'$ to indicate the normalized location of the zero points projected at the fluid−substrate interface, from the center (0) to the contact line (1) (eq 26). The $r'$ of the zero point indicates that this fluid


https://doi.org/10.1021/acsomega.3c03539
ACS Omega 2023, 8, 38991−39003

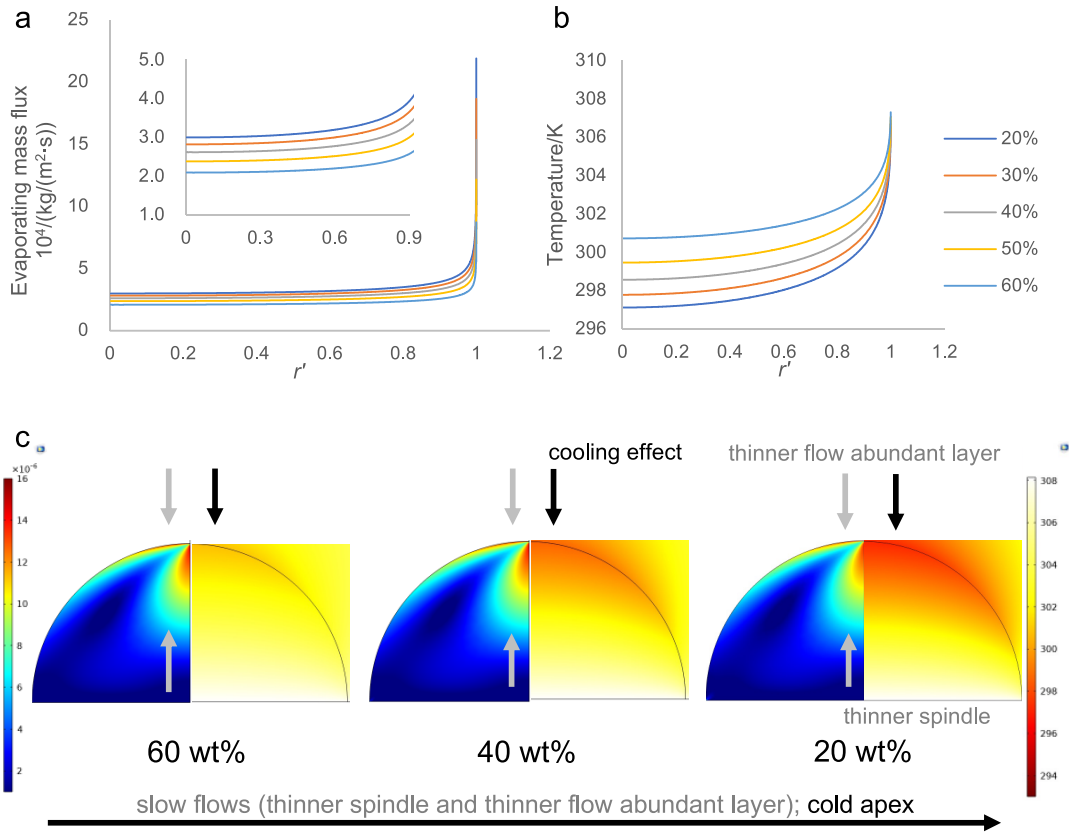


**Figure 7.** (a) Evaporating flux (kg·(m²·s)$^{-1}$) of droplets with different initial ethylene glycol concentrations, including 20, 30, 40, 50, and 60 wt %, evaporating at 308 K and $t'$ = 0.5. $r'$ represents the relative locations of the fluid−air interface from the apex (0) to the contact line (1). (b) Temperatures (K) at the fluid−air interface of the droplets in panel (a). (c) Velocity magnitude (left, m·s$^{-1}$) and temperature (right, K) of droplets with different initial ethylene glycol concentrations evaporating at 308 K and $t'$ = 0.5. The color bar on the left shows the ranges of velocity magnitude from $1.0 \times 10^{-6}$ m·s$^{-1}$ (dark blue) to $1.6 \times 10^{-5}$ m·s$^{-1}$ (dark red). The color bar on the right shows the temperature from 293 K (dark red) to 308 K (light yellow). The arrows point to the velocity peaks at the central apex, demonstrating their shrinking sizes (decelerating capillary flows) with increasing water concentration.

volume will be close to 0 once the fluid occupies an ample space like a high but narrow sandhill.

Correspondingly, a high ethylene glycol concentration will lower the zero-pointed $r'$ due to the robust circulating capillary flow, pushing the initial layer further inward. This $r'$ shows a zero point at 0.83 when the droplet has an initial 60 wt % ethylene glycol, while the zero point is at $r'$ = 0.94 when the droplet initially had 20 wt % (Figure 6a). All the droplets exhibited highly concentrated ethylene glycol at the bottom center, ranging from 80.3 to 97.3 wt %. When comparing the droplets in parallel, the concentrations at the center are directly related to the properties of the initial layers with ethylene glycol concentrations of 43.1, 52.9, 62.6, 72.4, and 82.1 wt % when the droplets initially contained 20, 30, 40, 50, and 60 wt %, respectively.

Similar phenomena also occurred when evaporating the droplet at different temperatures (303, 308, 313, and 318 K) (Figure 6b). The droplet evaporating at 318 K had a pure ethylene glycol area approximately at $r'$ = 0.6, while the concentration was 80 wt % at the exact location when evaporating at 303 K. The capillary flow was more robust to transport ethylene glycol sufficiently due to higher temperatures, leading to a more significantly piled fluid and smaller $r'$.

Ethylene glycol concentration increases at the bottom center with droplet evaporation (Figure 6c), but the mechanism differs from those in Figure 6a,b. The progressing evaporation decelerates the capillary flow because of the gradually uniform evaporation at the fluid−air interface. The decelerated capillary flow should have slowed the increasing rate of ethylene glycol concentration if the input fluid's content was constant. However, the concentration difference of ethylene glycol is more significant between $t'$ = 0.8 and $t'$ = 0.5 than between $t'$ = 0.5 and $t'$ = 0.2. The previously concentrated fluid increased the ethylene glycol concentration more effectively, although the capillary flow is weaker with progressing evaporation.

**Competing Factors Impacting Droplet Evaporation.** The simulation study shows four competing factors impacting the droplet evaporation of the $H_2O$−$(CH_2OH)_2$ mixture, including water concentration in the fluid, temperature, surface tension, and capillary flow. These four factors demonstrate a decreasing order of significance in enhancing the droplet evaporation rate. Water concentration is the most significant among the four factors enhancing droplet evaporation. The droplet evaporates faster with a higher water concentration, leading to a colder apex due to the cooling effect (Figure 7a). The low temperature decelerates the capillary flow, though the branched evaporating capillary flow is more robust, replenishing the fluid at the contact line. The flux is similar but rises quickly when approaching the contact line. The droplet, with 20 wt % ethylene glycol, exhibits a 50% higher flux than the droplet containing 60 wt % when $r'$ < 0.8. The differences are 65 and 250% when 0.8 < $r'$ < 0.9 and at the contact line ($r'$ =


https://doi.org/10.1021/acsomega.3c03539
ACS Omega 2023, 8, 38991−39003

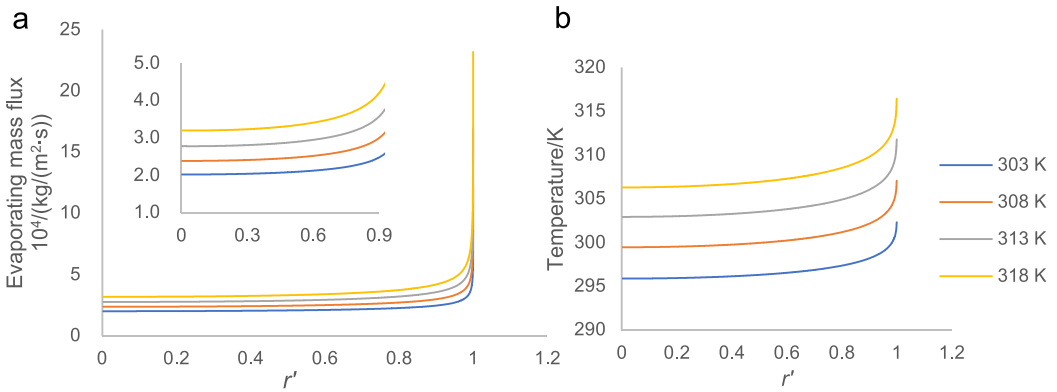


**Figure 8.** (a) Evaporating flux (kg·(m$^2$·s)$^{-1}$) and (b) temperature (K) at the fluid−air interface of droplets with an initial 50 wt % ethylene glycol, evaporating at different temperatures (303, 308, 313, and 318 K) and $t'$ = 0.5. The projected $r'$ ranges the relative locations of the fluid−air interface from the apex (0) to the contact line (1).

1), respectively. This study used $r'$ to illustrate the normalized location at the fluid−air interface, projecting at the fluid−substrate interface from the center (0) to the contact line (1).

The increasing water concentration introduces a cooling effect that decreases the fluid temperature at the apex (Figure 7b). This phenomenon occurs because the higher evaporating flux of water requires more heat to achieve the additional evaporation properties. The temperature difference is enlarged due to the colder apex, and consequently, the evaporation rate is lowered below that expected for a thoroughly heated fluid (Figure 4).

Figure 7c illustrates the droplets' velocity magnitude (left) and temperature (right) with different initial ethylene glycol concentrations, including 20, 40, and 60 wt %, evaporating at 308 K and $t'$ = 0.5. The velocity peak near the apex (gray arrows) is smaller, indicating the slower velocity circulating in the droplet with a lower ethylene glycol concentration. Furthermore, the tipping temperature decreases gradually with reduced ethylene glycol concentration (black arrows). Figure 7c confirms the cooling effect shown in Figure 7b, which decelerates the capillary flow with a decreasing ethylene glycol concentration. The water concentration dominates the droplet evaporation because the cold droplet and slow capillary flow do not favor increasing the evaporating flux.

The substrate temperature is the next vital factor for enhancing droplet evaporation, because the heat from the substrate allows water molecules to sufficiently diffuse from the droplet to the air. Similar to Figure 7a, the flux did not change significantly along most of the fluid−air interface but quickly rose near the contact line (Figure 8a). When $r'$ < 0.8, the evaporation at 318 K produces a 60% higher flux than at 303 K, but the difference increases by 374% at the contact line. Raising the temperature of the droplet fluid accelerates the competing capillary and Marangoni flows simultaneously. The simulation shows that the droplet evaporation increases with rising temperature, overcoming the competition between the Marangoni and capillary flows.

The heated substrate also exhibits a significant difference in temperature between the apex and the contact line due to the cooling effect and the natural convection with air (at ambient temperature) (Figure 8b). This result suggests that the simulated droplets showed a more substantial gap in the evaporation rates than those reported in ref 43 when the substrate temperature rose (Figure 4).

Changes in the surface tension will also overcome the competing capillary flows to enhance evaporation. In the simulation, the evaporating flux slightly increases with evaporation over time (Figure 9a). The COMSOL software incorporated surface tension changes at the fluid−air interface through its material modules, despite the simplified model geometry with a constant contact angle. The enhanced evaporation indicates that the lowered surface tension

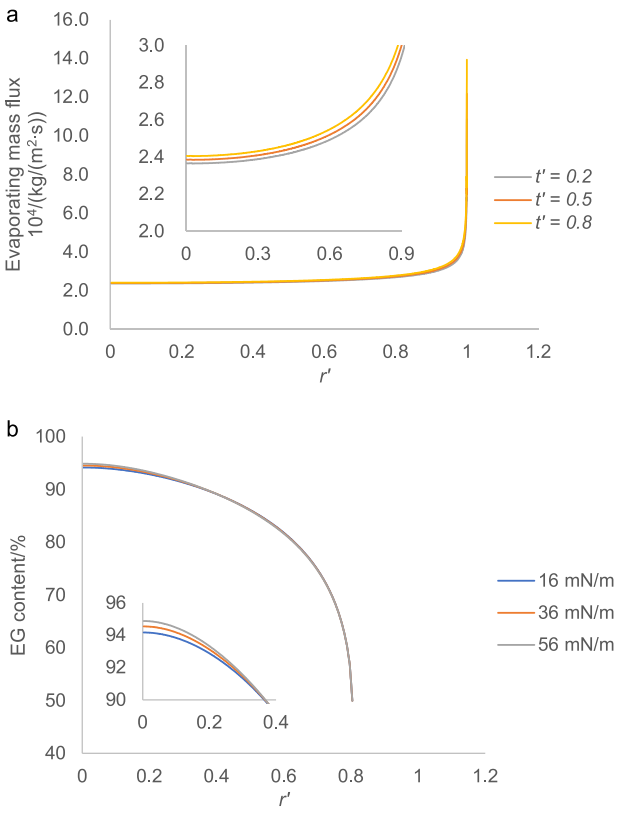


**Figure 9.** Influence of the initial surface tension on droplet evaporation with an initial 50 wt % ethylene glycol, evaporated at 308 K: (a) droplet evaporation (evaporating flux) (kg·(m$^2$·s)$^{-1}$) with the surface tension of the water−ethylene glycol mixture, as the droplet progresses (increasing $t'$); (b) ethylene glycol concentration (wt %) at the fluid−substrate interface when the droplets had a surface tension of 16, 36, and 56 mN·m$^{-1}$, $t'$ = 0.5. $r'$ represents the relative locations of the interfaces.



https://doi.org/10.1021/acsomega.3c03539
ACS Omega 2023, 8, 38991−39003

overcame the competing capillary flows. The ethylene glycol concentration at the fluid−substrate interface decreases slightly in the simulating droplets with a low initial surface tension (Figure 9b). However, the low surface tension suppresses the replenishing fluid from the apex to the contact line, decelerating the capillary flow behavior. As previously mentioned, the weakened circulating capillary flow accumulated ethylene glycol less sufficiently at the interface, especially at the bottom center.

Note that the model geometry with a constant contact angle will not significantly interfere with the mass transfer of ethylene glycol within the evaporating droplet when the initial surface tension is lowered (Figure 10). The simulations in this study assumed that the droplets had a constant contact angle of 90°, and the contact lines were unpinned during the evaporation (Figure 10a). The Marangoni vortices are thin at the fluid−air interface, even if a surfactant is added to lower the surface tension. The circulating capillary flow beneath the Marangoni vortices originates from heat transfer between the coldest apex and the hottest bottom center, which has the highest velocity (Figure 7c). It concentrates ethylene glycol at the bottom center in the "sandhill piling" mode, though less significantly with a lower surface tension.

The constant contact angle and unpinned contact line in the simulations are not critical in replicating natural evaporation because the evaporation of water−ethylene glycol mixtures does not change the geometric relationship between the Marangoni and capillary flows.[45] In natural evaporation, the contact angle is less than 90°, gradually decreasing due to the pinned contact line (Figure 10b). The Marangoni vortices change slightly with the fluid−air interface. Also, the slight contact angle suppresses the temperature difference between the apex and the bottom center, decelerating the circulating capillary flows beneath the Marangoni vortices. Still, the capillary flows dominate the microflows within the evaporating droplet on a heated substrate due to the fast water evaporation at the contact line, significantly replenishing the fluid from the apex to the contact line along the interface.

**Coffee-Ring Effect.** The COMSOL simulation of the $H_2O$−$(CH_2OH)_2$ ink solvent droplet evaporation recreated the experimentally observed coffee-ring effect where accumulated Ag particles settled along the contact line (Figure S7). During the thermally activated chemical reactions, the capillary flow dominates the particle transport within the droplet because the Marangoni flow (dotted red arrows) is weaker at the fluid−air interface due to the varied surface tension (Figure 11). The higher velocity region in the droplet (i.e., white dotted rectangles) indicates more vigorous flows at the contact line when evaporating at a higher temperature (318 than 308 K). The circulating capillary flow at the fluid−substrate interface is substantially smaller than at the upper regions of the droplet (green arrows). Due to the accumulation of ethylene glycol, the lower surface tension at the center of the droplet generates a Marangoni flow (dotted blue arrows) that moves toward the contact line. This Marangoni flow weakens the circulating capillary flow, resulting in a vortex at the fluid−substrate interface (black arrows).

In contrast, the microflows near the contact line are more significant because of the combined effect from the above Marangoni flows and the evaporating capillary flows. The fast evaporation at the contact line creates a vortex (solid red arrows) at the fluid−air interface near the contact line, because the resultant Marangoni flow (dotted red arrows) cancels the

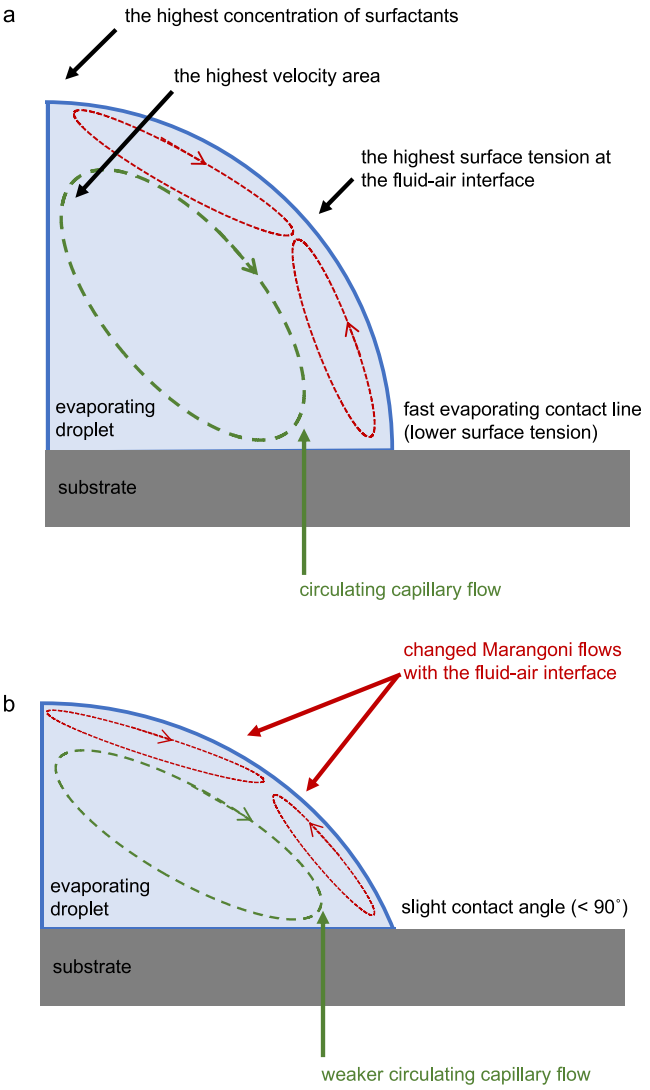


**Figure 10.** Microflows of an evaporating droplet with an added surfactant, assuming that (a) the droplet has a contact angle of 90° or (b) less than 90°, demonstrating natural evaporation. When adding a surfactant to the droplet, the highest surface tension occurs at the fluid−air interface between the apex and the contact line. Two thin Marangoni flows (red arrows) appear at the interface, indicating the highest surface tension point. The circulating capillary flow (green arrow) beneath the Marangoni vortices still drives the accumulation of ethylene glycol at the bottom center. The circulating capillary flow in panel (b) is weaker than those in panel (a); meanwhile, the capillary and Marangoni flows slightly change with the fluid−air interface of the evaporating droplet.

capillary flow. The higher temperatures at the vortex create a larger region in the droplet without significant fluid flow, because the Marangoni flow is more robust in this region. However, the computational simulation shows that the vortex is relatively small because the capillary flows at the upper interface overlap with Marangoni flows. Note that the fast water evaporation at the contact line dominates the microflows within the droplet evaporation of water−ethylene glycol mixtures (Figure 10b). The silver particles created from the chemical reactions are primarily transported throughout the droplet with the capillary flows, causing the smaller particles to be concentrated along the contact line, forming the coffee ring. Strengthening the Marangoni flow by adding surfactants does


https://doi.org/10.1021/acsomega.3c03539
ACS Omega 2023, 8, 38991−39003

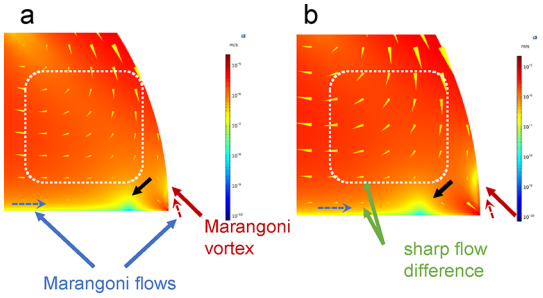


**Figure 11.** Velocity magnitude ($m{\cdot}s^{-1}$) near the contact line of droplets with an initial 50 wt % ethylene glycol, evaporating at (a) 308 and (b) 318 K, $t' = 0.9$. The color bar corresponds to the velocity ranges of the flows from $7.0 \times 10^{-11}$ $m{\cdot}s^{-1}$ (dark blue) to $2.2 \times 10^{-5}$ $m{\cdot}s^{-1}$(dark red). The cones indicate the flows with size and orientation. The red arrows indicate the Marangoni vortex at the fluid−air interface near the contact line.

not sufficiently suppress the coffee-ring effect (Figure S7), which was demonstrated by the COMSOL simulations. The analysis confirms that the capillary flows dominate the microflows within the evaporating droplets (Figures 9 to 11) and are largely responsible for Ag particle deposition on the substrate and the formation of the coffee-ring effect. Additional measures such as effective gelation[41] could limit the particles traveling within the capillary flows and help eliminate the formation of the ring (Figure S1). Furthermore, higher temperatures could strengthen the gelation process, which immobilizes the particles and, thereby, generates a smoother film surface at an appropriate temperature. However, the impact of gelation is beyond the scope of this study and was not incorporated into the computational analysis.

## CONCLUSIONS

In this work, the authors numerically simulated the droplet evaporation of the reactive ink solvent ($H_2O$−$(CH_2OH)_2$ mixture) on a heated substrate. An ethylene glycol-accumulated layer appears at the fluid−substrate interface when initially evaporating the droplets. The oval-circulating capillary flow transported the collected ethylene glycol from this layer toward the bottom center like piling sand on a hill. The droplet evaporation relied on various factors, including water concentration, substrate temperatures, surface tension, and capillary flow. These four factors were in decreasing order of significance in enhancing the evaporation process. The simulations also showed that the capillary flow dominated the fluid−substrate and fluid−air interfaces, leading to the coffee-ring effect at the contact line. These results provided new insights into the droplet reactions of the reactive silver ink, as the simulation demonstrated sufficient clues on heat and mass transfer during evaporation. Limiting the speed of evaporation is essential to improving the quality of the inkjet-printed pattern. The gentle capillary flows help suppress the coffee-ring effect, producing a smooth silver film. The low substrate temperature limits the ethylene glycol concentration in initial layer to uniform the droplet's surface tension, weakening the capillary and Marangoni flows. However, the model's geometric error limited the ability of the simulation methodology to accurately collect the information on the fluid−air interface.

## ASSOCIATED CONTENT

### Supporting Information

The Supporting Information is available free of charge at https://pubs.acs.org/doi/10.1021/acsomega.3c03539.

Photographs of the Ag particle morphology within the droplet film (S1), droplet separation in inkjet printing applications (S2), and the coffee-ring effect of the reactive Ag ink droplet (S7); additional discussion on error analysis of the simulations (S3), concentration of $(CH_2OH)_2$ along the central axis of the droplet (S4), velocity magnitude within the evaporating droplet (S5), and demonstration of the zero point in the $(CH_2OH)_2$ accumulation model (S6) (PDF)

## AUTHOR INFORMATION

### Corresponding Author

**George K. Knopf** − *Mechanical and Materials Engineering, The University of Western Ontario, N6A 5B9 London, Ontario, Canada;* orcid.org/0000-0002-8696-9247; Email: gknopf@uwo.ca

### Authors

**Weipeng Zhang** − *Mechanical and Materials Engineering, The University of Western Ontario, N6A 5B9 London, Ontario, Canada;* orcid.org/0009-0002-7081-5742

**Jun Yang** − *Mechanical and Materials Engineering, The University of Western Ontario, N6A 5B9 London, Ontario, Canada; Shenzhen Institute for Advanced Study, University of Electronic Science and Technology of China, 518110 Shenzhen, Guangdong, China;* orcid.org/0000-0002-7545-4213

Complete contact information is available at: https://pubs.acs.org/10.1021/acsomega.3c03539

### Notes

The authors declare no competing financial interest.

## ACKNOWLEDGMENTS

G.K.K. would like to thank Natural Sciences and Engineering Research Council of Canada (NSERC grant RGPIN/04797-2022) for funding. J.Y. would like to thank Natural Sciences and Engineering Research Council of Canada (NSERC grant RGPIN/05198-2016) and Goodwin Technology (H.K.) Co., Ltd., for funding. Portions of this research were carried out with the support of the staff at Surface Science Western (SSW). All authors would like to thank C.M.C. Microsystems for providing valuable simulation support.

## REFERENCES

(1) Brenn, G.; Deviprasath, L. J.; Durst, F.; Fink, C. Evaporation of acoustically levitated multi-component liquid droplets. *Int. J. Heat Mass Transfer* **2007**, *50*, 5073−5086.

(2) Zhu, P.; Zhang, H.; Lu, H. Preparation of polyetherimide nanoparticles by a droplet evaporation-assisted thermally induced phase-separation method. *Polymers* **2021**, *13*, 1548.

(3) Kuznetsov, G. V.; Misyura, S. Y.; Volkov, R. S.; Morozov, V. S. Marangoni flow and free convection during crystallization of a salt solution droplet. *Colloids Surf. A Physicochem. Eng. Asp.* **2019**, *572*, 37−46.

(4) Malla, L. K.; Bhardwaj, R.; Neild, A. Colloidal deposit of an evaporating sessile droplet on a non-uniformly heated substrate. *Colloids Surf. A Physicochem. Eng. Asp.* **2020**, *584*, No. 124009.

(5) Li, Y.; Diddens, C.; Lv, P.; Wijshoff, H.; Versluis, M.; Lohse, D. Gravitational effect in evaporating binary microdroplets. *Phys. Rev. Lett.* **2019**, *122*, No. 114501.
(6) Wu, M.; Doi, M.; Man, X. The contact angle of an evaporating droplet of a binary solution on a super wetting surface. *Soft Matter* **2021**, *17*, 7932−7939.
(7) Zhou, P.; Yu, H.; Zou, W.; Wang, Z.; Liu, L. High-resolution and controllable nanodeposition pattern of Ag nanoparticles by electro-hydrodynamic jet printing combined with coffee ring effect. *Adv. Mater. Interfaces* **2019**, *6*, 1900912 DOI: 10.1002/admi.201900912.
(8) Black, K.; Singh, J.; Mehta, D.; Sung, S.; Sutcliffe, C.; Chalker, P. Silver ink formulations for sinter-free printing of conductive films. *Sci. Rep.* **2016**, *6*, 1−7, DOI: 10.1038/srep20814.
(9) Shahariar, H.; Kim, I.; Soewardiman, H.; Jur, J. S. Inkjet printing of reactive silver ink on textiles. *ACS Appl. Mater. Interfaces* **2019**, *11*, 6208−6216.
(10) Agrawal, A.; Gopu, M.; Mukherjee, R.; Mampallil, D. Microfluidic droplet cluster with distributed evaporation rates as a model for bioaerosols. *Langmuir* **2022**, *38*, 4567−4577.
(11) Nanlohy, H. Y.; Wardana, I. N. G.; Hamidi, N.; Yuliati, L.; Ueda, T. The effect of $Rh^{3+}$ catalyst on the combustion characteristics of crude vegetable oil droplets. *Fuel* **2018**, *220*, 220−232.
(12) Goh, G. L.; Saengchairat, N.; Agarwala, S.; Yeong, W. Y.; Tran, T. Sessile droplets containing carbon nanotubes: A study of evaporation dynamics and CNT alignment for printed electronics. *Nanoscale* **2019**, *11*, 10603−10614.
(13) Shin, Y. E.; Cho, J. Y.; Yeom, J.; Ko, H.; Han, J. T. Electronic textiles based on highly conducting poly (vinyl alcohol)/carbon nanotube/silver nanobelt hybrid fibers. *ACS Appl. Mater. Interfaces* **2021**, *13*, 31051−31058.
(14) Zhang, Z.; Zhang, X.; Xin, Z.; Deng, M.; Wen, Y.; Song, Y. Controlled inkjetting of a conductive pattern of silver nanoparticles based on the coffee-ring effect. *Adv. Mater.* **2013**, *25*, 6714−6718.
(15) Zheng, X.; Zhu, Y.; Liu, Y.; Zhou, L.; Xu, Z.; Feng, C.; Zheng, C.; Zheng, Y.; Bai, J.; Yang, K.; Zhu, D.; Yao, J.; Hu, H.; Zheng, Y.; Guo, T.; Li, F. Inkjet-printed quantum dot fluorescent security labels with triple-level optical encryption. *ACS Appl. Mater. Interfaces* **2021**, *13*, 15701−15708.
(16) Duan, Y.; Zhang, G.; Yu, R.; Zhang, H.; Niu, G.; Huang, Y.; Yin, Z. Inkjet printing for scalable and patterned fabrication of halide perovskite-based optoelectronic devices. *J. Mater. Chem. C* **2022**, *10*, 14379−14398.
(17) Ryu, B. H.; Choi, Y.; Park, H. S.; Byun, J. H.; Kong, K.; Lee, J. O.; Chang, H. Synthesis of highly concentrated silver nanosol and its application to inkjet printing. *Colloids Surf., A* **2005**, *270*, 345−351.
(18) Zhou, Y.; Xu, Z.; Bai, H.; Knapp, C. E. Room temperature electronic functionalization of thermally sensitive substrates by inkjet printing of a reactive silver-based MOD ink. *Adv. Mater. Technol.* **2023**, *8*, 2201557.
(19) Deroco, P. B.; Wachholz Junior, D.; Kubota, L. T. Silver inkjet-printed electrode on paper for electrochemical sensing of paraquat. *Chemosensors* **2021**, *9*, 61.
(20) Stempien, Z.; Rybicki, E.; Rybicki, T.; Lesnikowski, J. Inkjet-printing deposition of silver electro-conductive layers on textile substrates at low sintering temperature by using an aqueous silver ions-containing ink for textronic applications. *Sens. Actuators, B Chem.* **2016**, *224*, 714−725.
(21) Finn, D. J.; Lotya, M.; Coleman, J. N. Inkjet printing of silver nanowire networks. *ACS Appl. Mater. Interfaces* **2015**, *7*, 9254−9261.
(22) Dong, Y.; Li, X.; Liu, S.; Zhu, Q.; Li, J. G.; Sun, X. Facile synthesis of high silver content MOD ink by using silver oxalate precursor for inkjet printing applications. *Thin Solid Films* **2015**, *589*, 381−387.
(23) Khan, Z.; Al-Thabaiti, S. A.; Obaid, A. Y.; Khan, Z. A.; Al-Youbi, A. O. Effects of solvents on the stability and morphology of CTAB-stabilized silver nanoparticles. *Colloids Surf., A* **2011**, *390*, 120−125.
(24) Wang, J.; Chen, Z.; Hu, Y.; Jiang, X.; Chen, D.; Zhang, W. Flaky silver powders prepared with nanofilm transition method: application for printable electronics. *J. Mater. Chem. C* **2013**, *1*, 230−233.
(25) Wang, Y.; Du, D.; Zhou, Z.; Xie, H.; Li, J.; Zhao, Y. Reactive conductive ink capable of in situ and rapid synthesis of conductive patterns suitable for inkjet printing. *Molecules* **2019**, *24*, 3548.
(26) Dustov, M.; Golovina, D. I.; Polyakov, A. Y.; Goldt, A. E.; Eliseev, A. A.; Kolesnikov, E. A.; Sukhorukova, I. V.; Shtansky, D. V.; Grünert, W.; Grigorieva, A. V. Silver eco-solvent ink for reactive printing of polychromatic SERS and SPR substrates. *Sensors* **2018**, *18*, 521.
(27) Thayyil Raju, L.; Diddens, C.; Li, Y.; Marin, A.; Van Der Linden, M. N.; Zhang, X.; Lohse, D. Evaporation of a sessile colloidal water-glycerol droplet: Marangoni ring formation. *Langmuir* **2022**, *38*, 12082−12094.
(28) Weon, B. M.; Je, J. H. Capillary force repels coffee-ring effect. *Phys. Rev. E* **2010**, *82*, No. 015305.
(29) Jiang, C.; Zhong, Z.; Liu, B.; He, Z.; Zou, J.; Wang, L.; Wang, J.; Peng, J.; Cao, Y. Coffee-ring-free quantum dot thin film using inkjet printing from a mixed-solvent system on modified ZnO transport layer for light-emitting devices. *ACS Appl. Mater. Interfaces* **2016**, *8*, 26162−26168.
(30) Misyura, S. Y.; Kuznetsov, G. V.; Feoktistov, D. V.; Volkov, R. S.; Morozov, V. S.; Orlova, E. G. The influence of the surface microtexture on wettability properties and drop evaporation. *Surf. Coat. Technol.* **2019**, *375*, 458−467.
(31) Volkov, R. S.; Strizhak, P. A. Research of temperature fields and convection velocities in evaporating water droplets using planar laser-induced fluorescence and particle image velocimetry. *Exp. Therm. Fluid Sci.* **2018**, *97*, 392−407.
(32) Bozorgmehr, B.; Murray, B. T. Numerical simulation of evaporation of ethanol-water mixture droplets on isothermal and heated substrates. *ACS Omega* **2021**, *6*, 12577−12590.
(33) Li, Y.; Chen, Z.; Liang, D.; Zang, J.; Song, Z.; Cai, L.; Zou, Y.; Wang, X.; Wang, Y.; Li, P.; Gao, X.; Ma, Z.; Mu, X.; El-Shaer, A.; Xie, L.; Su, W.; Song, T.; Sun, B. Coffee-stain-free perovskite film for efficient printed light-emitting diode. *Adv. Opt. Mater.* **2021**, *9*, 2100553 DOI: 10.1002/adom.202100553.
(34) Inanlu, M. J.; Farhadi, J.; Ansari, E.; Charkas, S.; Bazargan, V. Effect of surfactant concentration on the evaporation-driven deposition of carbon nanotubes: from coffee-ring effect to strain sensing. *RSC Adv.* **2022**, *12*, 31688−31698.
(35) Zaibudeen, A. W.; Bandyopadhyay, R. Formation and development of distinct deposit patterns by drying polyelectrolyte-stabilized colloidal droplets at different surfactant concentrations. *J. Mol. Liq.* **2022**, *367*, No. 120355.
(36) Gao, A.; Liu, J.; Ye, L.; Schönecker, C.; Kappl, M.; Butt, H. J.; Steffen, W. Control of droplet evaporation on oil-coated surfaces for the synthesis of asymmetric supraparticles. *Langmuir* **2019**, *35*, 14042−14048.
(37) Liu, Y.; Pan, J.; Hu, Z.; Chu, Y.; Khan, M. S.; Tang, K.; Guo, L.; Lau, C. Stability improvement for dried droplet pretreatment by suppression of coffee ring effect using electrochemical anodized nanoporous tin dioxide substrate. *Microchim. Acta* **2020**, *187*, 1−10, DOI: 10.1007/s00604-020-04640-w.
(38) Al-Milaji, K. N.; Zhao, H. New perspective of mitigating the coffee-ring effect: interfacial assembly. *J. Phys. Chem. C* **2019**, *123*, 12029−12041.
(39) Raghuram, G. K.; Bansal, L.; Basu, S.; Kumar, A. Suppression of coffee ring effect in high molecular weight polyacrylamide droplets evaporating on hydrophobic surfaces. *Colloids Surf., A* **2021**, *612*, No. 126002.
(40) Shimobayashi, S. F.; Tsudome, M.; Kurimura, T. Suppression of the coffee-ring effect by sugar-assisted depinning of contact line. *Sci. Rep.* **2018**, *8*, 17769 DOI: 10.1038/s41598-018-35998-w.
(41) Zhu, Z.; Ning, H.; Cai, W.; Wei, J.; Zhou, S.; Yao, R.; Lu, X.; Zhang, J.; Zhou, Z.; Peng, J. Morphology modulation of direct inkjet printing by incorporating polymers and surfactants into a sol-gel ink system. *Langmuir* **2018**, *34*, 6413−6419.


https://doi.org/10.1021/acsomega.3c03539
*ACS Omega* 2023, 8, 38991−39003

(42) Stempien, Z.; Rybicki, E.; Patykowska, A.; Rybicki, T.; Szynkowska, M. I. Shape-programmed inkjet-printed silver electro-conductive layers on textile surfaces. *J. Ind. Text.* **2018**, *47*, 1321−1341.
(43) Rusdi, M.; Moroi, Y.; Nakahara, H.; Shibata, O. Evaporation from water- ethylene glycol liquid mixture. *Langmuir* **2005**, *21*, 7308−7310.
(44) Spees, W. M.; Song, S. K.; Garbow, J. R.; Neil, J. J.; Ackerman, J. J. Use of ethylene glycol to evaluate gradient performance in gradient-intensive diffusion MR sequences. *Magn. Reson. Med.* **2012**, *68*, 319−324.
(45) Farhadi, J.; Bazargan, V. Marangoni flow and surfactant transport in evaporating sessile droplets: A lattice Boltzmann study. *Phys. Fluids* **2022**, *34*, No. 032115, DOI: 10.1063/5.0086141.



https://doi.org/10.1021/acsomega.3c03539
*ACS Omega* 2023, 8, 38991−39003